Safer Formulation Concept for Flame-Generated Engineered Nanomaterials

Samuel Gass,[†,‡] Joel M. Cohen,[†] Georgios Pyrgiotakis,[†] Georgios A. Sotiriou,[†,‡] Sotiris E. Pratsinis,[‡] and Philip Demokritou*,[†]

[†]Center for Nanotechnology and Nanotoxicology at Harvard School of Public Health, Harvard University, 665 Huntington Avenue, 02115 Boston, Massachusetts, United States

[‡]Particle Technology Laboratory, Institute of Process Engineering, Department of Mechanical and Process Engineering, Swiss Federal Institute of Technology Zurich (ETH Zurich), Sonneggstrasse 3, CH-8092, Zurich, Switzerland

S *Supporting Information*

ABSTRACT: The likely success or failure of the nanotechnology industry depends on the environmental health and safety of engineered nanomaterials (ENMs). While efforts toward engineering safer ENMs are sparse, such efforts are considered crucial to the sustainability of the nanotech industry. A promising approach in this regard is to coat potentially toxic nanomaterials with a biologically inert layer of amorphous SiO_2. Core−shell particles exhibit the surface properties of their amorphous SiO_2 shell while maintaining specific functional properties of their core material. A major challenge in the development of functional core−shell particles is the design of scalable high-yield processes that can meet large-scale industrial demand. Here, we present a

safer formulation concept for flame-generated ENMs based on a one-step, in flight SiO_2 encapsulation process, which was recently introduced by the authors as a means for a scalable manufacturing of SiO_2-coated ENMs. First, the versatility of the SiO_2-coating process is demonstrated by applying it to four ENMs (CeO_2, ZnO, Fe_2O_3, Ag) marked by their prevalence in consumer products as well as their range in toxicity. The ENM-dependent coating fundamentals are assessed, and process parameters are optimized for each ENM investigated. The effects of the SiO_2-coating on core material structure, composition, and morphology, as well as the coating efficiency on each nanostructured material, are evaluated using state-of-the-art analytical methods (XRD, N_2 adsorption, TEM, XPS, isopropanol chemisorption). Finally, the biological interactions of SiO_2-coated vs uncoated ENMs are evaluated using cellular bioassays, providing valuable evidence for reduced toxicity for the SiO_2-coated ENMs. Results indicate that the proposed "safer by design" concept bears great promise for scaled-up application in industry in order to reduce the toxicological profile of ENMs for certain applications.

KEYWORDS: *Safer nanoformulations, Flame-generated nanomaterials, Nanotechnology, Nanotoxicology, Core−shell particles*
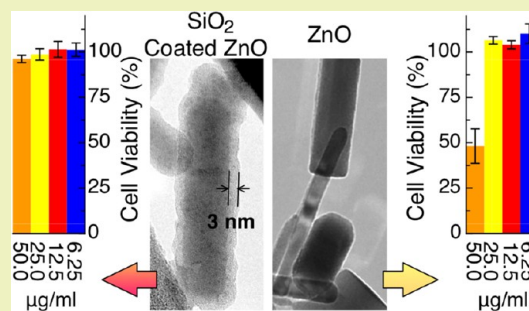
The global nanotechnology industry reached over 1.5 trillion USD last year and has become a major economic force in the 21st century.[1] Engineered nanomaterials (ENMs) are by far the largest segment of the nanotechnology market, accounting for 80% of all revenues.[2] Global ENM production rates are expected to increase by more than 20 times within the next 15 years.[3] Meanwhile, the number of consumer products containing ENMs is growing at a similarly exponential pace.[4] ENMs are found in products ranging from sunscreens and cosmetics to food and beverages, building materials, and toner formulations, making human and environmental exposure inevitable.[5,6] Preliminary evidence demonstrates the potential for ENMs to cause adverse biological effects.[7] Nanosized particles (NPs) may enter cells and exhibit greater toxic potential than their micrometer-sized counterparts due to their small size and corresponding large surface to volume ratio.[7] The potential of nanoparticles and nanofibers to translocate across air−blood barriers, accessing critical extrapulmonary organs is also of concern.[8−11]

While significant research has been directed toward understanding nano-bio interactions (SG), research toward devising safer ENM formulation concepts that can readily be adopted by the nanotechnology industry is very sparse.[12,13] A promising approach in this regard is coating potentially toxic nanomaterials with a nanothin layer of amorphous SiO_2. Amorphous SiO_2 is considered a biologically and environmentally inert material, often used as a negative control material in in vitro ENM screening assays.[14] Such nanothin SiO_2 is therefore ideal to shield otherwise potentially toxic core-materials from any interactions with environmental and biological systems. The "core−shell" ENMs exhibit the surface properties of their shell while preserving certain important intrinsic functional proper-
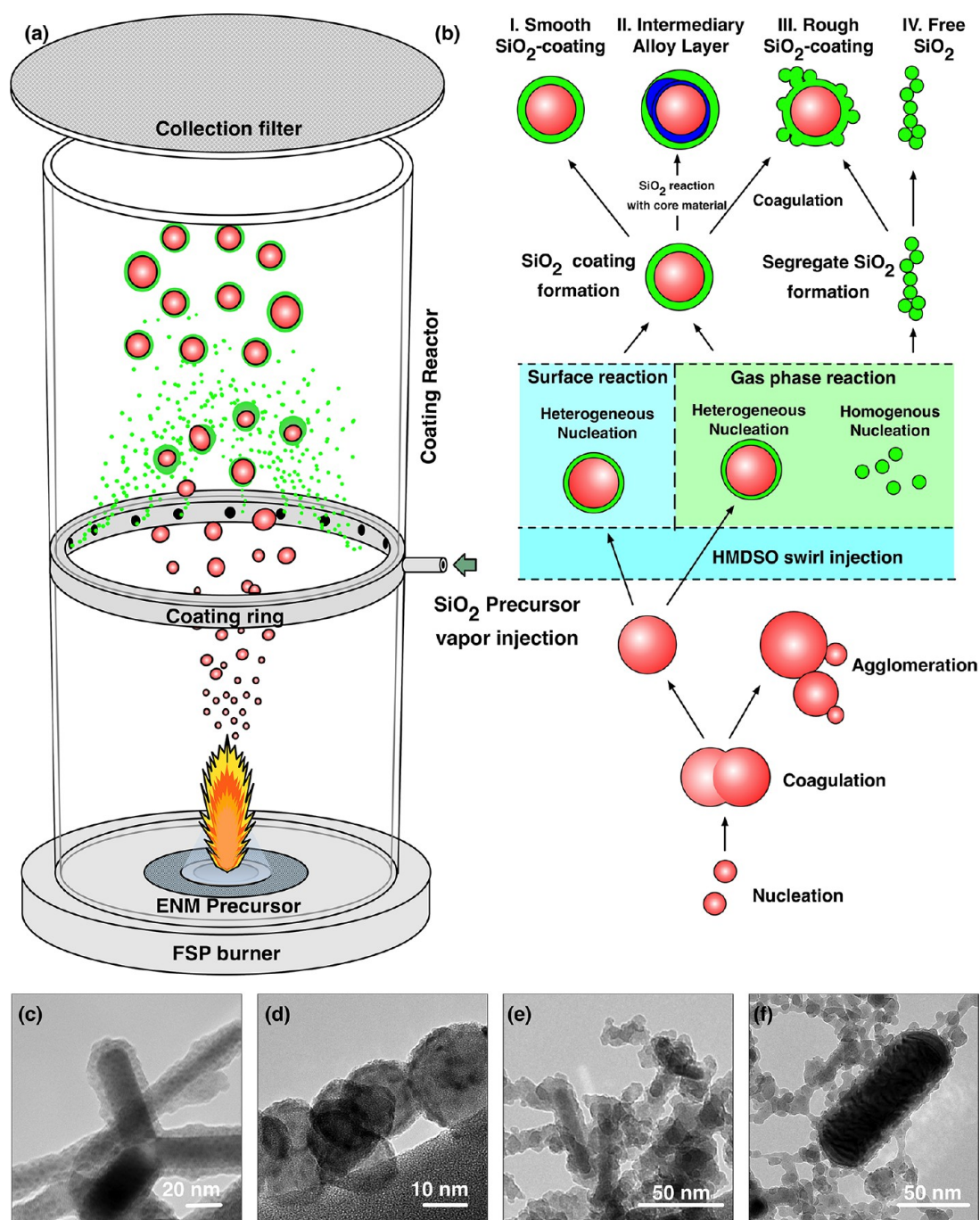
Figure 1. ENM synthesis and SiO$_2$ coating fundamentals. (a) Schematic of the coating reactor highlighting the most important elements. Core ENMs are formed through the combustion of organometallic compounds dissolved in high enthalpy solvents. The HMDSO vapor is injected into the particulate flow in an in-line SiO$_2$-coating reactor. (b) Mechanism of the coating and the possible results. The high temperatures obtained in the core particle synthesis provide the necessary energy for the HMDSO conversion to SiO$_2$ vapor. Under optimal SiO$_2$ vapor supersaturation conditions, the SiO$_2$ vapor nucleates heterogeneously onto the core ENM surface, thereby forming a desired SiO$_2$-coating layer of controlled thickness (case I). The ENM specific optimization of the coating reactor temperature and mixing profiles is required in order to prevent the following: (1) surface reactions between the core material and the SiO$_2$ vapor (alloying) (case II), (2) homogeneous SiO$_2$ nucleation which may result in segregated SiO$_2$ domains and/or rough surface coatings (case III), and (3) inhomogeneous SiO$_2$ coatings (patchy coatings) or free silica (case IV). The above-discussed cases are representatively shown for the coating of ZnO: smooth coating (c), alloying (forming of zinc silicates, zinc oxide, and silica) (d), rough coating (e), and free (segregated) silica formation (f).

ties (i.e., optical,[15] magnetic properties,[16,17] plasmonic,[18] phosphorescence[19]) of their core materials.

Here, a "safer formulation concept" based on this SiO$_2$ coating process is presented. By design, this concept is tailored to a family of ENMs with the highest volume of production,[20] namely, flame-generated nanomaterials. Gas phase (flame

aerosol) processes are the preferred routes for scalable ENM synthesis as they do not create liquid byproducts, offer easier particle collection from gases than liquids, usually include fewer process steps, and result in high purity materials with unique morphologies including the synthesis of metastable phases.[21,22] The applied SiO$_2$-coating process in flames has major

advantages over wet methods, such as sol−gel[23,24] and reverse microemulsion[25] which are frequently applied to the synthesis of SiO$_2$-coated nanoparticles by industry. These low-yield, multistep, wet synthesis methods often produce porous SiO$_2$ coatings,[26] which cannot sufficiently protect surrounding media from any potential toxic implications of the core materials.

In this study, a flame spray pyrolysis ENM synthesis platform (VENGES)[27,28] recently developed by the authors was modified to allow for in-flight coating of ENMs with a nanothin layer of amorphous SiO$_2$.[15] This flame-based SiO$_2$-coating process has recently been explored by the authors as a means of high-yield scalable nanomanufacturing of SiO$_2$-coated ENMs such as TiO$_2$, Fe$_2$O$_3$, and Ag. However, its versatility as well as the implication of the SiO$_2$-coating on the toxicological profiles of these particles were never investigated. Herein, we showcase the versatility of the SiO$_2$-coating process by applying it to a comprehensive and industry-relevant nanopanel (CeO$_2$, Fe$_2$O$_3$, ZnO, Ag). ENMs were chosen based on their range in toxicity[29] and prevalence in consumer products.[4] Moreover, we characterize the effect of the SiO$_2$-coating on core material structure, composition, and morphology, as well as the coating efficiency of the process using state-of-the-art analytical methods. Finally, the influence of surface coating on ENM− biological interactions is evaluated using several in vitro bioassays and cellular toxicity is assessed.

■ RESULTS AND DISCUSSION

SiO$_2$-Encapsulation Strategy: Coating Reactor. Figure 1a and b illustrates the proposed approach and underlying theory to the one-step nanoparticle synthesis and in-flight SiO$_2$-encapsulation, respectively. As presented in detail in the Materials and Methods section, core nanoparticles are formed in the gas phase by flame spray pyrolysis of organometallic compounds dissolved in high enthalpy solvents.[30] The freshly formed core nanoparticles pass through the SiO$_2$ coating region, where they are encapsulated with a nanothin (1−5 nm) amorphous SiO$_2$ layer by the swirl-injection of hexamethyldisiloxane (HMDSO) vapor-laden N$_2$.

The key to successful hermetic coatings is to reduce the temperature in the coating region as to inhibit further core particle growth, maintaining however, sufficient temperatures for the conversion of HMDSO to SiO$_2$-coatings (heterogeneous nucleation). The quality of SiO$_2$-coating on the core nanoparticles is influenced mainly by the coating reactor temperature profile, the mixing profile of the SiO$_2$ precursor vapor with the core nanoparticles, and the HMDSO injection molar flow rate. This has previously been described by the authors for the case of SiO$_2$-coated TiO$_2$.[15]

Figure 1c−f representatively shows particle morphology of SiO$_2$-coated ZnO synthesized for different process parameters and illustrates the effect of various process parameters on the coating efficiency (Supporting Information Table S1). For example, in the case of ZnO, when using xylene as the high enthalpy solvent in the core particle synthesis step, the temperature profile in the SiO$_2$-coating zone is very high (>1500 K). This leads to a reaction between the core ZnO nanoparticles and the SiO$_2$ coating, thereby forming substoichiometric zinc silicates (Zn$_{1.7}$SiO$_4$, XRD, Supporting Information Figure S3) on the surface of the ZnO core nanoparticles (dark spots in Figure 1d). However, by carefully selecting a solvent with lower specific combustion enthalpy density (here ethanol), the zinc silicate formation can be

inhibited and a homogeneous smooth nanothin SiO$_2$-coating is obtained (Figure 1c).

Varying molar flow rate ratio of the amount of HMDSO vapor that is injected to the one of the core materials ($\dot{n}_{HMDSO}/\dot{n}_{core}$) enables precise control over the SiO$_2$-coating thickness.[15,16,18] However, if this ratio or the absolute HMDSO concentration in the reactor is increased over a certain threshold, the HMDSO vapor can nucleate homogenously, thereby forming segregated SiO$_2$. This results in some core ZnO nanoparticles that are fully coated with SiO$_2$ but also free SiO$_2$ nanoparticles (Figure 1e and f). These separate SiO$_2$ nanoparticles may further sinter with the SiO$_2$-coated ZnO ENMs forming rather rough SiO$_2$ surface coatings (Figure 1e). The particular temperature profile is also likely responsible for various combinations of these possibilities.

From the aforementioned examples, it is evident that the process is highly core ENM material-dependent and therefore needs to be optimized for each case individually. For the purpose of this study, ENM-dependent process parameters related to synthesis of all ENMs were optimized in order to enable complete encapsulation of the core ENMs with a smooth SiO$_2$ nanothin layer of a controlled thickness, avoiding the generation of free-standing SiO$_2$ and rough SiO$_2$ surfaces, as will be presented in the section below.

Effect of SiO$_2$-Coating on Core Material Structure and Composition. The effect of the SiO$_2$ coating on the core material was investigated with transmission electron microscopy (TEM) for the overall structural properties. X-ray diffraction (XRD) was used to assess the crystal structure of the materials, and nitrogen absorption via the Brunauer−Emmett−Teller (BET) method was used to examine the specific surface area.

Figure 2 shows TEM images of the resulting bare and SiO$_2$-coated ENMs for each of the ENMs in the study (CeO$_2$, Fe$_2$O$_3$, Ag, and ZnO). The amorphous,[16−18,31,32] smooth, and relatively homogeneous SiO$_2$ layer (2−5 nm) around each material is indicative of optimal synthesis parameters (Supporting Information Table S1). As shown in Figure 2, the core nanoparticles form agglomerated and/or aggregated chainlike structures, which is typical with gas phase synthesis of nanostructured materials. Therefore, the SiO$_2$-coating also encapsulates these agglomerates rather than individual core nanoparticles.[18] The characteristic shape of the primary particles (CeO$_2$ polyhedral, Fe$_2$O$_3$ hexagonal, Ag spherical, ZnO rodlike), however, is unaltered by the smooth SiO$_2$-coating (Figure 2). The absence of segregated free SiO$_2$ domains or co-oxidized SiO$_2$-core material particles is indicative of the evenly distributed heterogeous nucleation onto the entire core ENM particle surface.

Figure 3 illustrates the effect of increased HMDSO injection volume ($\dot{n}_{HMDSO}/\dot{n}_{core}$), which corresponds to a specific theoretical coating thickness (TCT, upper axis in Figure 3a−d), on core particle crystal structure and size, as measured by X-ray diffraction (XRD), as well as composite particle specific surface area (SSA), measured by N$_2$ adsorption (BET). It is worth noting that the TCT is estimated based on the $\dot{n}_{HMDSO}/\dot{n}_{core}$ flow ratio, assuming full HMDSO conversion to an anhydrous and perfectly dense SiO$_2$-coating, as well as spherical primary particles of a known diameter (d_{XRD}) and is just an indicator of how much HMDSO injection volume was used. On the basis of these parameters and assumptions, the TCT can be calculated as follows:
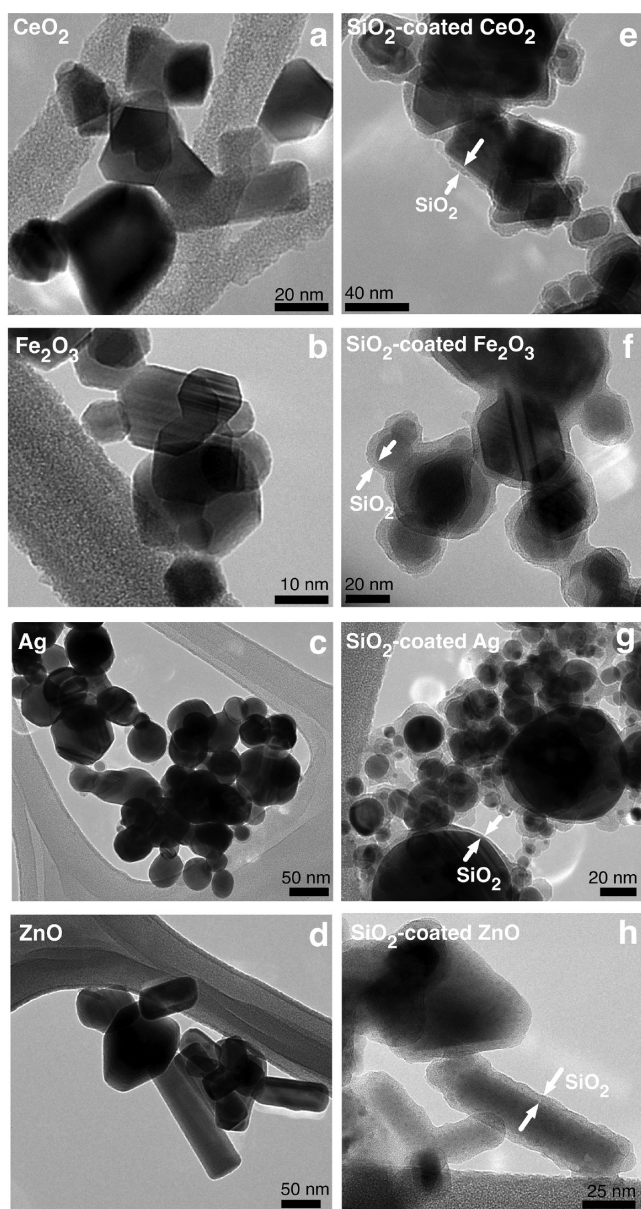
Figure 2. TEM images of bare (a–d) and SiO$_2$-coated (e–h) CeO$_2$, Fe$_2$O$_3$, Ag, and ZnO. The SiO$_2$-coating layer (2–5 nm) appears as a lighter contrast contour around stronger contrast core particles.

$$\text{TCT} = \left[\left(\frac{2\text{MW}_{\text{SiO}_2}\dot{n}_{\text{HMDSO}}\rho_{\text{core}}}{\text{MW}_{\text{core}}\dot{n}_{\text{core}}\rho_{\text{SiO}_2}} + 1 \right)^{1/3} - 1 \right] \frac{d_{\text{XRD}}}{2} \quad (1)$$

where TCT is the theoretical coating thickness, $\dot{n}_{\text{HMDSO}}$ is the HMDSO injection rate [mol/s], MW$_{\text{SiO}_2}$ is the molecular weight of SiO$_2$ [g/mol], MW$_{\text{core}}$ is the molecular weight of core material [g/mol], ρ_{SiO_2} is the density of SiO$_2$ [g/cm^3], ρ_{core} is the density of core material [g/cm^3], and d_{XRD} is the XRD determined crystal size.

For increasing HMDSO injection molar flow rate (increased TCT), the average crystal sizes of CeO$_2$ (a), Fe$_2$O$_3$ (b), and ZnO (d) remained constant indicating that core-particle growth was minimal at the point of HMDSO injection. This is in agreement with previous studies for the case of SiO$_2$-coated TiO$_2$[15] and Fe$_2$O$_3$.[16] Therefore, for the materials used in this study (CeO$_2$, Fe$_2$O$_3$, ZnO), the process enabled independent control over primary particle size and SiO$_2$-coating thickness. In the case of Ag, crystal size decreased progressively with increased HMDSO injection volume (Figure 3c). This indicates that the growth of Ag is not terminated at the HMDSO injection point, likely attributable to the low melting point of silver. However, with an increasing $\dot{n}_{\text{HMDSO}}/\dot{n}_{\text{core}}$ flow ratio, the core nanosilver size decreases, exhibiting further the core size tuneability as shown in previous studies.[18]

Assessing Segregated SiO$_2$ Formation during the Coating Process. The SSA of SiO$_2$-coated CeO$_2$ and SiO$_2$-coated Fe$_2$O$_3$ remained constant when increasing the HMDSO injection volume, indicating minimal separate SiO$_2$ nanoparticle formation and surface roughness (Figures 3a and b). Free SiO$_2$ formation would lead to larger SSA (>100 m^2/g).[15,33] In the cases of both Ag and ZnO (Figures 3c and d); however, an increase in SSA is observed for higher HMDSO injection volumes, which would indicate the formation of separate SiO$_2$ nanoparticles or rough surface coatings.[34] However, TEM images of SiO$_2$-coated Ag (Figure 2g) reveal minimal free SiO$_2$ nanoparticle formation. Therefore, such increase in SSA for SiO$_2$-coated nanosilver might also stem from (i) the large density difference between Ag and SiO$_2$, (ii) the decrease in Ag primary particle sizes, and (iii) an increase in SiO$_2$ surface roughness with increased HMDSO injection molar flow rate. In the case of ZnO (Figure 3d), the formation of segregated (free) SiO$_2$ was also observed beyond a certain HMDSO injection volume ($\dot{n}_{\text{HMDSO}}/\dot{n}_{\text{core}} > 0.2$). This is also evident from the high SSA obtained for $\dot{n}_{\text{HMDSO}}/\dot{n}_{\text{core}} > 0.2$ (105 m^2/g, Figure 3d) as well as TEM images (Figure 1c) of this sample. Higher HMDSO concentrations can lead to the spontaneous (homogeneous) nucleation of SiO$_2$ due to oversaturation as well as insufficient core material surface for heterogeneous nucleation and needs to be avoided as part of the optimization process for each ENM.[31]

In conclusion, for all ENMs investigated, SiO$_2$-encapsulation showed no significant effect on the crystal structure and composition of the core material. The locations of X-ray diffraction peaks of the SiO$_2$-coated materials coincide with those of the bare materials (Figure 3e). Some minor differences in diffraction patterns for the case of Fe$_2$O$_3$ might be attributed to the formation of α-Fe$_2$O$_3$ ([104] plane peak which appears suppressed in the presence of SiO$_2$). In the case of Ag, as explained above, the SiO$_2$-coating leads to smaller Ag crystal sizes, broadening the characteristic diffraction peaks of metallic silver (Figure 3e). It should also be noted that the absence of crystalline SiO$_2$ peaks in the XRD patterns is a clear indication that the SiO$_2$ formed under these conditions is indeed amorphous. This is very important for the toxicological profile of SiO$_2$, as it is known in the literature that crystalline SiO$_2$ is highly toxic.[35]

Assessing Coating Quality. TEM imaging was utilized to evaluate coating uniformity, coating roughness, and the formation of free silica. To confirm the absence of the free silica, the specific surface area was also measured. As described in the previous section, SiO$_2$ has a very high surface area (~200 m^2/g) as compared to the core particles (30–50 m^2/g), and therefore, the presence of free silica will immediately increase the specific surface area of the coated particles compared to that of the uncoated ones. We also employed isopropanol chemisorption as an additional qualitative method to monitor reactions that are catalyzed only by the core material, ensuring that the particles are completely coated.
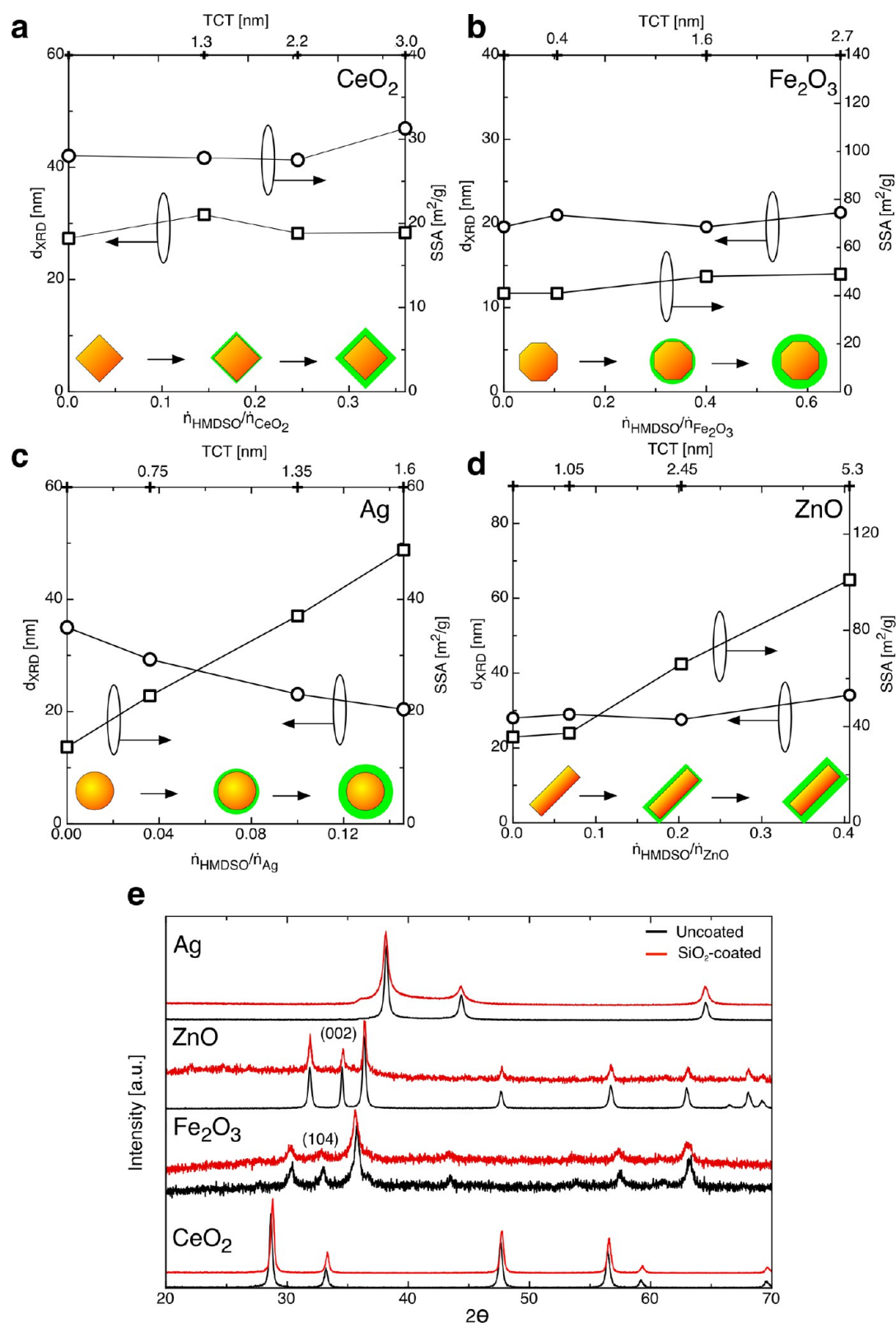
Figure 3. SSA $[m^2/g]$ (right axis) and crystal size [nm] (left axis) of SiO_2-coated CeO_2 (a), Fe_2O_3 (b), Ag (c), and ZnO (d) as a function of core particle to HMDSO molar ratio ($\dot{n}_{HMDSO}/\dot{n}_{core}$) (lower axis) and theoretical coating thickness (TCT) (upper axis). (e) XRD patterns of bare (black) and SiO_2-coated (red) ENMs.

X-ray photoelectron spectroscopy (XPS) was used to assess the coating quality quantitatively. XPS has very short penetration depth, ~5 nm, and therefore scans only the upper most atomic layers of the nanoparticles.[36−38] In the case

that the coating is sufficient in thickness, the only XPS peaks detected will be SiO_2 peaks. Typically, however, electrons with lower binding energy have higher kinetic energy, increasing therefore their inelastic mean free path (IMFP), giving strong
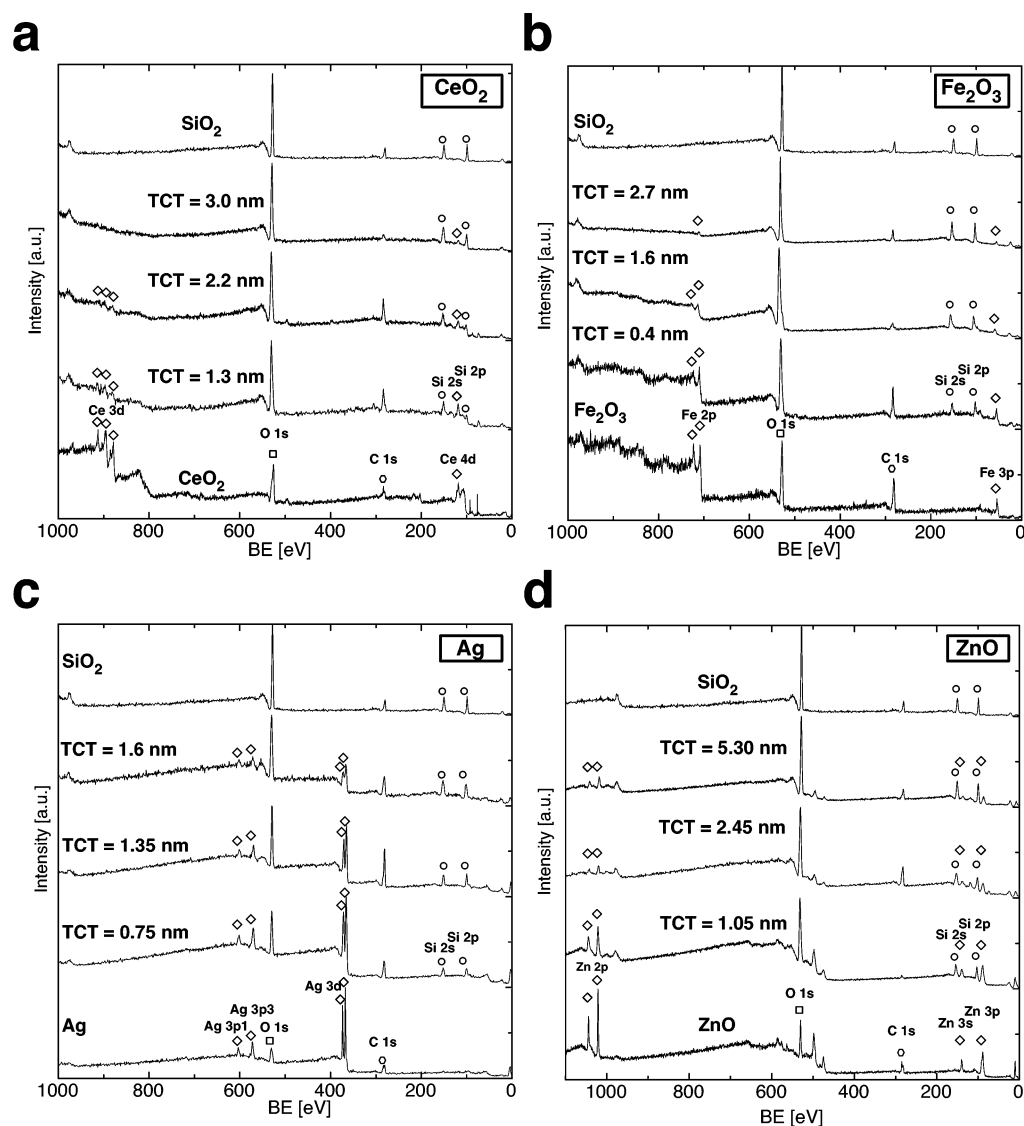
Figure 4. Coating efficiency: XPS survey spectra of bare and SiO$_2$-coated CeO$_2$ (a), Fe$_2$O$_3$ (b), Ag (c), and ZnO (d). Spectra shown for increasing TCTs. Pure SiO$_2$ (upper most spectrum) included for reference purposes.

signal even for coatings thicker than 5 nm.[39] Additionally, the peak intensity depends on the relative surface area of silica to the core material. It is therefore likely that the presense of free SiO$_2$ can give false results by increasing the silica signal, even for partially coated core particles. Therefore XPS was always assessed in conjuction with SSA data and the TEM imaging, in order to rule out the free SiO$_2$ scenario.

As previously discussed, the TEM and SSA measurements confirmed both the uniform smooth coating of the ENMs (TEM, Figure 2e−h) and the lack of surface area increase (BET, Figure 3a−d), clear indications of minimum free SiO$_2$ formation. Moreover, Figures 4a−d show the XPS survey spectra of the materials investigated with increasing SiO$_2$-coating thickness as defined by the theoretical coating thickness (TCT, explained in detail in the Materials and Methods section). For each spectrum shown, core metal electron transitions as well as Si and O electron transitions are highlighted with diamond, circles, and squares, respectively. With increasing TCT values, the XPS survey spectra (Figures 4a−d) of the ENMs showed a rapid decrease in the core metal electron peaks (for the peaks with the higher binding energy)

and a corresponding increase in the Si electron transitions. In the case of CeO$_2$ and Fe$_2$O$_3$, the spectrum of SiO$_2$-coated CeO$_2$ (TCT = 3.0 nm) and SiO$_2$-coated Fe$_2$O$_3$ (TCT = 2.7 nm) matches that of the pure SiO$_2$, clearly indicating a hermetic encapsulation of the ENMs. For Ag and ZnO, the characteristic core metal electron peaks remain visible, even for the highest TCT, but the TEM shows a smooth uniform coating for both cases. This is attributed to low binding energy electrons coming from the bulk material, which still make it through the SiO$_2$ layer.[40] Similarly the low binding energy peaks of Ce in Figure 4a are still present even when the higher binding energy peaks have disappeared. As a result, a portion of the core electron peaks observed for small TCTs (1−2 nm) does, in fact, stem from core electrons below the SiO$_2$ coating layer and not because of the lack of hermetic coating.

The XPS spectra can also be used to quantify the hermetic coating nature of ENMs.[37,38] Here, the following elemental ratio X_{el} metric is proposed and defined as the ratio of the core material elemental concentration to the total elemental concentration (eq 2):
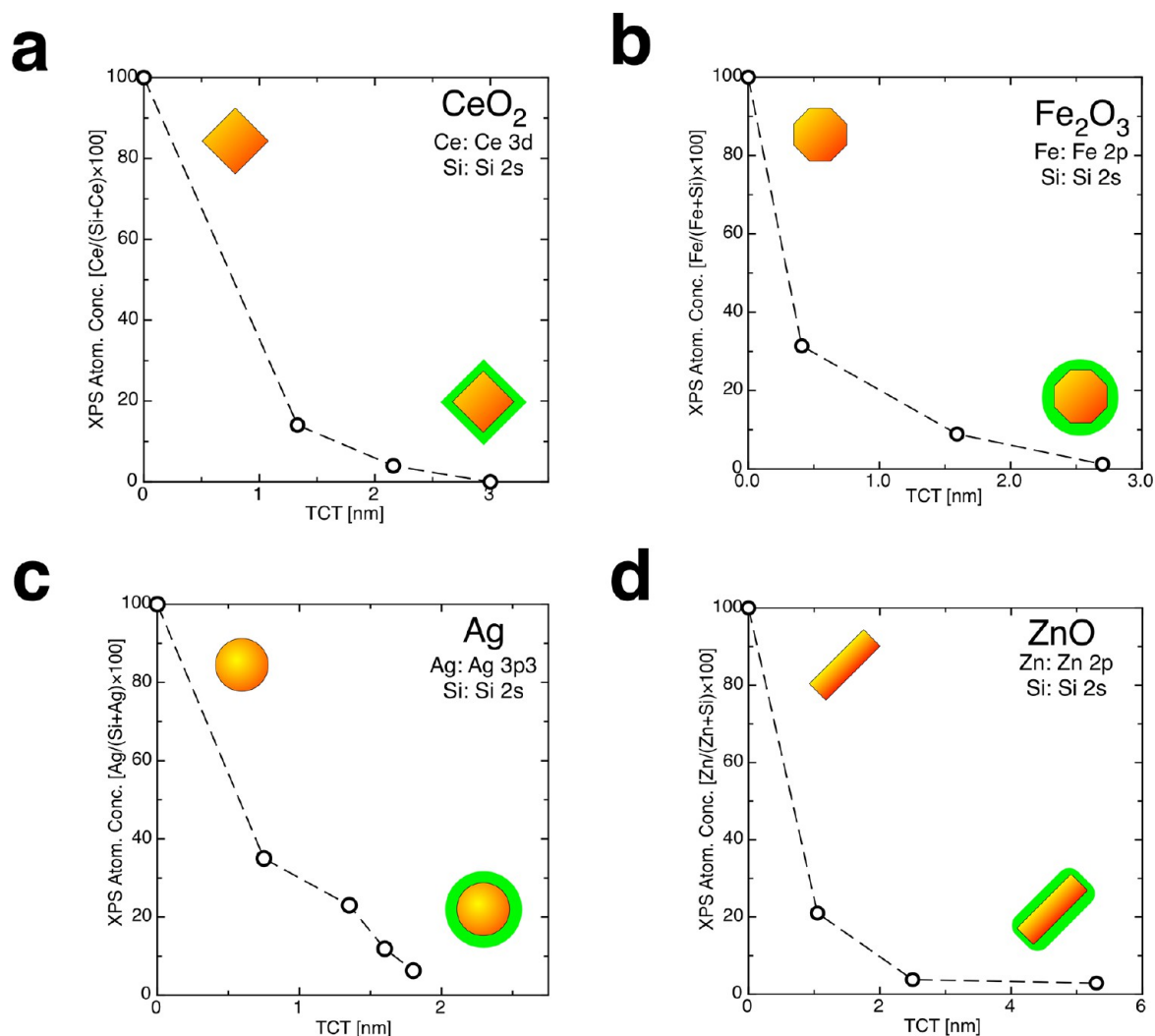
Figure 5. XPS surface atomic concentration ratio $[Me_{core}/(Me_{core} + Si)]$ for bare and SiO_2-coated ENMs as a function of TCT [nm].
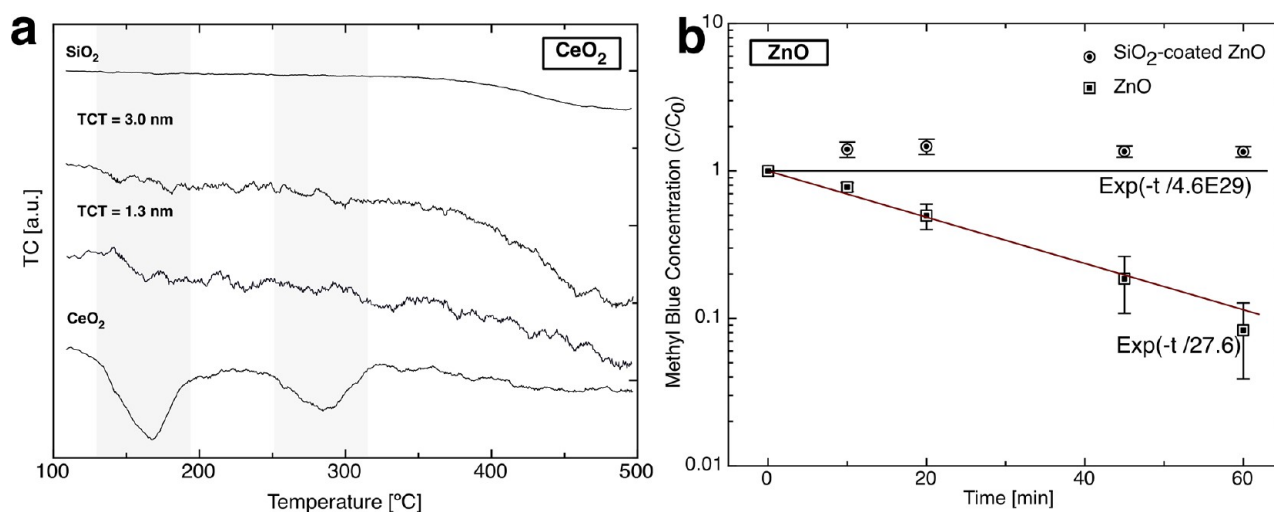
Figure 6. Off-gas thermal conductivity (TC) as a function of temperature during isopropanol desorption from pure SiO_2, SiO_2-coated CeO_2, and bare CeO_2 (a). Concentration of methylene blue in aqueous solutions measured by optical absorption spectra in the presence of ZnO and SiO_2-coated ZnO nanoparticles under UV irradiation (254 nm) for varying time (b).

$$X_{el} = \frac{Me_{core}}{Me_{core} + Si} \qquad (2)$$

where Me_{core} and Si are the core-material and silicon elemental concentration, respectively. For elements having more than one binding energy peak, the highest one is regarded. Figure 5

849

dx.doi.org/10.1021/sc300152f | *ACS Sustainable Chem. Eng.* 2013, 1, 843−857

Table 1. Summary of ENMs (Bare and SiO$_2$-Coated) Used to Evaluate ENM−Cellular Interactions^a

material	theoretical SiO$_2$ [wt%]	TCT [nm]	$d_{XRD,core}$	SSA [m^2/g]	d_H (nm)		ζ (mV)
SiO$_2$	100	N/A	19 (d_{BET})	147	DI H$_2$O	192 ± 9.183	−28.4 ± 6.90
					F12K/3%FBS	192 ± 3.032	−9.73 ± 2.84
CeO$_2$	0	0	28	32.8	DI H$_2$O	225.6 ± 2.56	37.8 ± 1.85
					F12K/3%FBS	183.7 ± 2.42	−12.5 ± 0.289
SiO$_2$-coated CeO$_2$	20	3	31	37	DI H$_2$O	215.2 ± 2.75	−38.4 ± 1.86
					F12K/3%FBS	226.9 ± 3.16	−11.6 ± 0.451
Fe$_2$O$_3$	0	N/A	19.6	42	DI H$_2$O	163.1 ± 49.0	40.7 ± 17.6
					F12K/3%FBS	1063 ± 79.15	−10.1 ± 1.45
SiO$_2$-coated Fe$_2$O$_3$	33	2.7	21.3	49	DI H$_2$O	248.8 ± 2.1	−53.6 ± 19.9
					F12K/3%FBS	966.2 ± 77.8	−11.4 ± 1.54
Ag	50	N/A	20.4	57	DI H$_2$O	152.4 ± 1.48	−19.5 ± 1.31
					F12K/3%FBS	332.2 ± 7.63	−11 ± 0.551
SiO$_2$-coated Ag	10	1.8	28	29	DI H$_2$O	219.9 ± 1.9	−18.5 ± 1.5
					F12K/3%FBS	255.2 ± 3.16	−11.6 ± 0.153
ZnO	0	N/A	28	36	DI H$_2$O	218.4 ± 3.9	23.0 ± 0.462
					F12K/3%FBS	199.8 ± 8.42	−9.89 ± 2.05
SiO$_2$-coated ZnO	23	2.5	27.0	66	DI H$_2$O	164.9 ± 1.71	−15.9 ± 1.27
					F12K/3%FBS	207.5 ± 4.05	−11.1 ± 0.814

^{a}Note: The high hydrodynamic diameter of the Fe$_2$O$_3$ nanoparticles in biological medium are likely attributable to the interparticle magnetic attractive forces.[45−47]

shows corresponding X_{el} derived from the XPS survey spectra as a function of TCT for all four different materials (a−d). As expected, the X_{el} decreases rapidly as a function of TCT for all materials investigated.[15] It must be noted, however, that the XPS probing depth can be a few nanometers deep. For cases in which the TCT is between 0 and 2 nm, a fraction of electrons from the core material may still be ejected. However, XPS cannot distinguish if these electrons originate from core electrones penetrating through the SiO$_2$ coating or uncoated areas on the particle surface. Therefore, we expect the proposed metric to underestimate the coating efficiency of certain materials when the TCT is inferior to the core electron IMFP. However, in our case, the optimum SiO$_2$ coating thickness is greater than 2 nm; therefore, the XPS data can be used to demonstrate quantitatively the hermetic nature of SiO$_2$ coating for all particles.

In order to further eliminate the possibility of patchy coatings, and to cross validate the XPS coating efficiency data, isopropanol chemisorption[16] on SiO$_2$-coated and bare CeO$_2$ particles was performed. Since the chemisorption of iso-propanol on SiO$_2$ is minimal, no sharp drop in thermal conductivity (TC) is visible for the SiO$_2$ curve (Figure 6a). In contrast, two pronounced peaks (shaded regions) were seen for bare CeO$_2$ (165 and 283 °C). The first may be attributed to the release of adsorbed isopropanol or surface reaction products, as it corresponds fairly well to the surface isopropoxide decomposition temperature of 190 °C.[41] The second peak may be attributed to other, more tightly adsorbed, isopropanol decomposition products.[42] For an increasing SiO$_2$ TCT up to 3 nm, the peaks almost disappear and only very small bands are visible. Even at TCT of 1.3 nm, ENM samples show no significant reduction in TC at the expected desorption temperatures, indicating minimal bare CeO$_2$ surface.

Furthermore, the coating efficiency on the core ZnO nanoparticles was evaluated by monitoring methylene blue degradation in aqueous solution in the presence of ZnO nanoparticles and UV light (254 nm). Uncoated ZnO nanoparticles are photocatalytic nanoparticles that can degrade organic dyes, such as methylene blue.[43] Such methylene blue

degradation can be seen in Figure 6b, where the normalized methylene blue concentration (C/C_0) is plotted as a function of time in the presence of uncoated (circles) and SiO$_2$-coated ZnO nanoparticles (squares) and UV light (254 nm). In the case of the uncoated ZnO nanoparticles, the methylene blue concentration decreases over time, indicating its degradation because of the photocatalytic ZnO surface. However, in the presence of the SiO$_2$-coated ZnO nanoparticles the methylene blue concentration in solution remains rather constant over time, indicating the minimal photocatalytic activity of those nanoparticles. This further verifies that the ZnO core nanoparticles are fully coated. Both the isopropanol chem-isorption and the photocatalytic activity data results are in agreement with the XPS data, a clear indication that the proposed use of XPS spectra as a means to quantify the coating quality is valid.

In conclusion, the aforementioned results demonstrate the ability of this scalable process to hermetically coat a wide range of ENMs. Moreover, the particular combination of character-ization methods applied to evaluating the coatings (BET, TEM, XPS, and isopropoanol chemisorption) enables an accurate qualitative and quantitative indication of the coating efficiency.

While this study focuses on the environmental health and safety implications of the SiO$_2$-coated ENMs, the resulting coated particles have great potential for many other applications. It is worth mentioning that SiO$_2$ surface can be easily further functionalized to facilitate dispersibility in liquids and other possible applications in nanomedicine.

Effect on SiO$_2$ Coatings on Core Material Functional Properties. It has been shown in other recently published studies by the authors that a nanothin layer of SiO$_2$ coating can maintain other specific optical,[15] plasmonic,[18] phosphores-cent,[33] and magnetic[16] properties of the core ENM. This is essential for the whole safer formulation concept, as the target is to maintain the desirable inherent core ENM specific functional properties and simultaneously exploit the surface properties of SiO$_2$ as well as inhibit any toxicological outcomes. However, this approach cannot be considered a "swiss army knife" for all ENMs and all applications. For example, coating
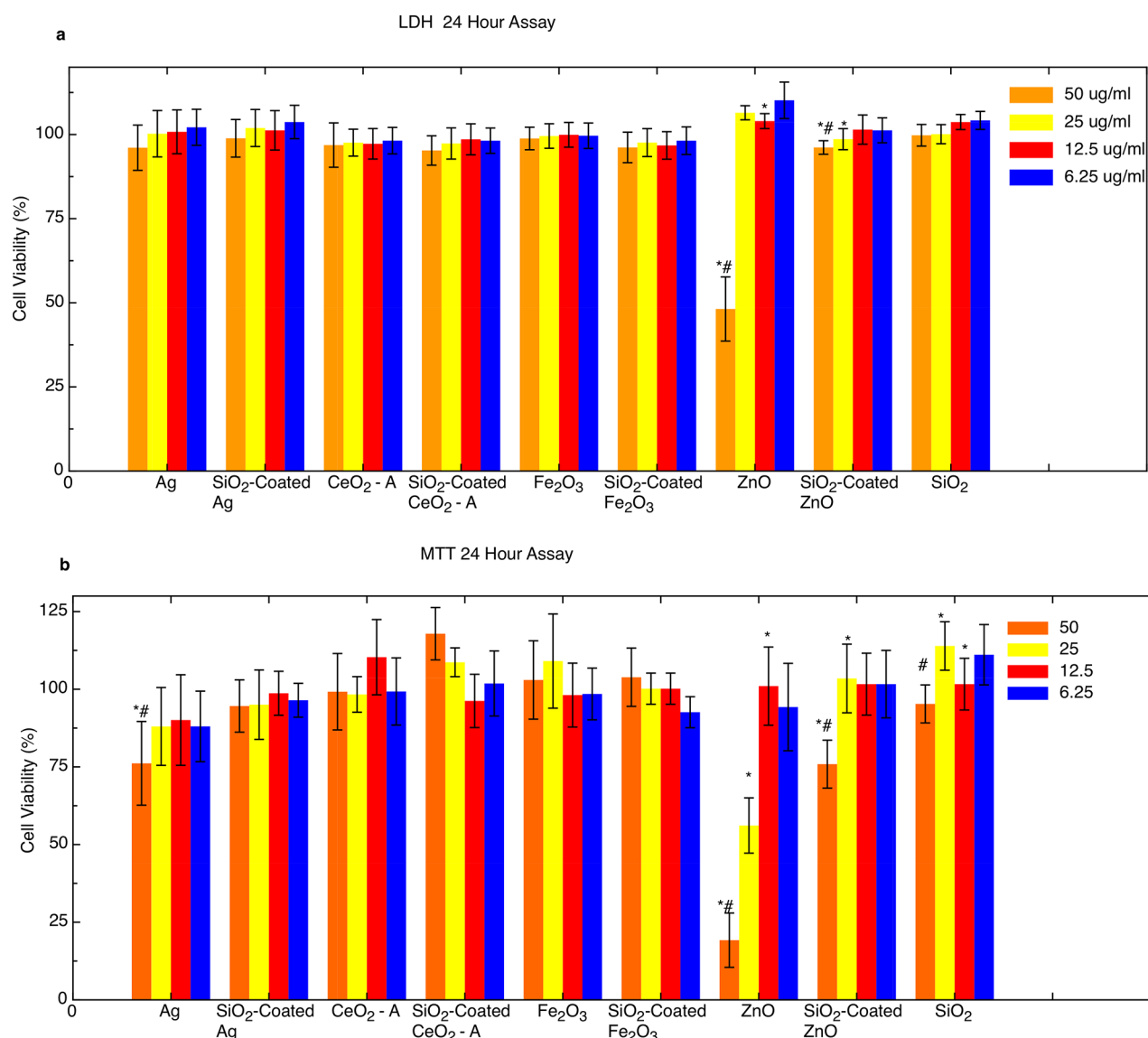
Figure 7. Cytotoxicity as measured by LDH (a) and MTT (b) absorbance after 24 h exposures to 0–50 ug/mL bare and SiO$_2$-coated Ag, CeO$_2$, Fe$_2$O$_3$, ZnO, and pure SiO$_2$ (left to right) in A549 cells. (#) values for each dose are not all equal (ANOVA) for $p < 0.05$; (*) significantly different from immediate right neighbor for $p < 0.05$.

the surface with amorphous SiO$_2$ will likely eliminate the desirable catalytic properties of CeO$_2$, or bactericidal properties of Ag associated with their specific chemistries. On the contrary, coating Ag surface with SiO$_2$ used for plasmonic applications while reducing ion leaching and toxicological outcomes may be beneficial.

In this study, we selected to showcase the minimal effect of SiO$_2$ coating on optical properties of ZnO. Both the coated and uncoated ZnO ENMs demonstrated a similar ultraviolet A (UVA) absorbance peak around 370 nm (Supporting Information, Figure S-1), clear indication of no change on the optical properties. Therefore, the SiO$_2$ coated ZnO prepared with this high yield scalable nanomanufacturing process makes it ideal for use in cosmetics and sunscreens. It is worth making the point here, that this proposed approach for a safer formulation of ZnO is preferable to other proposed safer formulation approaches such as Fe doping ZnO ENMs to reduce Zn solubility, as such doping ultimately alters the optical properties of ZnO.[13] Thus, such hermetically SiO$_2$-coated ZnO

nanoparticles could be used in specific applications as UV-filters (e.g., in sunscreens) without compromising their desired performance while reducing their toxicity, as it will be demonstrated in sections below.

Effect of SiO$_2$ Coating on ENM-Biological Interactions. *Characterization of ENM Behavior When Suspended in Physiological Media.* The hydrodynamic diameter and zeta potential of all uncoated and SiO$_2$-coated ENMs under study dispersed in both deionized (DI) H$_2$O and in physiological media commonly used for cellular bioassays, are summarized in Table 1 (see the Materials and Methods section for dispersion protocol details). The zeta-potential measured for all four SiO$_2$-coated ENMs dispersed in DI H$_2$O were strongly negative and comparable to that of bare SiO$_2$.[44] These values were distinct from the strongly positive values, measured for their uncoated counterparts with the exception of Ag (Table 1).[44] Furthermore, all SiO$_2$-coated ENMs exhibit similar agglomeration in deionized (DI) water and match that of pure SiO$_2$ particles of same primary particle size and were stable over the

851

dx.doi.org/10.1021/sc300152f | *ACS Sustainable Chem. Eng.* 2013, 1, 843–857

course of 24 h. This is another confirmation for the successful encapsulation of ENMs by SiO_2.

In addition, in physiologic media used in cellular bioassays, protein adsorption to the nanoparticle surface strongly influenced agglomeration state and is reflected in the measured hydrodynamic diameter and zeta-potential (Table 1). This is in agreement with previously reported studies.[44] The high hydrodynamic diameter of the Fe_2O_3 nanoparticles in biological medium are likely attributable to the interparticle magnetic attractive forces.[45−47]

ENM−Cellular Interactions. The biologically inert nature of amorphous SiO_2 ENMs has been reported in a number of recently published in vitro studies.[48,49] However conflicting evidence has also been reported, identifying silanol groups on the surface of amorphous SiO_2 ENMs as key mediators that can induce hemolysis[50] as well as alveolar epithelial cell toxicity at high doses.[51] In vivo the anti-inflammatory nature of amorphous SiO_2 is documented in a number of studies,[52,53] providing supportive evidence for our "safer-formulation" approach. Sayes et al. reported short-term acute aerosol exposures produced no significant pulmonary inflammatory, genotoxic, or adverse lung histopathological effects in rats, even at very high doses up to 86 mg/m^3.[53]

It is worth mentioning the different pulmonary responses associated with crystalline, colloidal, or amorphous silica dusts.[35] It was shown that amorphous SiO_2 induced a low and transient pulmonary inflammatory response in rats, whereas crystalline silica induced large and persistent pulmonary inflammatory responses.[35] Synthetic amorphous silica, including colloidal, precipitated, and, as in our case, fumed silica, is not involved in progressive fibrosis of the lung.[54,55] However, high doses of amorphous silica may result in acute pulmonary inflammatory responses in exposed animals.[56] Impurities on the surface of amorphous SiO_2 particles may lead to the formation of highly toxic silanes with implications for cellular viability. However, there are no impurities or silanes on the surface of the flame generated SiO_2-coated particles as shown by our XPS data, which is also in agreement with thermogravimetric analyses of the surface chemistry of fumed silica particles previously reported in the literature.[57] While more research is needed to clearly identify and characterize the health risks associated with respiratory exposure to amorphous fumed SiO_2, current evidence suggests those risks are minimal.[52]

The role of the SiO_2 surface coatings on ENM−cell interactions, and its effect on biological properties, was assessed in this study using human alveolar basal epithelial A549 cells and two different commonly used bioassays (LDH absorbance, a measure of cytotoxicity, and MTT absorbance, a measure of cell viability, see the Materials and Methods section for details). Figure 7a and b report cell viability for A549 cells exposed to varied doses of a liquid ENM dispersions (0−50 $\mu g/mL$) after 24 h exposure, for both bare and SiO_2-coated ENMs.

As shown in Figure 7, at the doses investigated, exposure to pure SiO_2 resulted in no significant decrease in cell viability as measured by our LDH and MTT assays (Figure 7a and b). Additionally, SiO_2-coated ZnO nanoparticles show reduced toxicity compared to their bare counterparts, further indication of the hermetic nature of the coating (Figure 7a and b).

Recently published studies also report that amorphous SiO_2 is relatively insoluble in both water and in various cell culture media,[49] suggesting the ENMs under study remain encapsulated in a layer of relatively inert SiO_2.

ENM−Cellular Interactions: Reduction of Toxicity for the Case of ZnO. As shown in Figure 6, exposure to uncoated ZnO nanoparticles resulted in significant decreases in cell viability as measured by our LDH and MTT assays (Figure 7a and b). Our results are consistent with previously reported studies demonstrating that nanosized ZnO particles exert toxicity in mammalian cells, as measured by lysosomal damage, mitochondrial perturbation, reactive oxygen species generation, induction of pro-inflammatory cytokine release, and cell death.[58,59] In addition, recent studies investigating the effects of nanosized ZnO in vivo report substantial lung inflammatory responses including LDH release and recruitment of poly-morphonuclear monocytes (PMNs) in rats following intra-tracheal instillation.[12,60] As shown in Figure 7a and b, the SiO_2 encapsulation effectively increased cell viability (p value < 0.05), especially at higher administered doses. This protective effect is likely due to inhibition of Zn ion leaching into the cellular environment,[12] thereby minimizing cytotoxicity. Therefore, the dissolution of ZnO is inhibited by the presence of the hermetic SiO_2 coating, and the nanoparticle toxicity is reduced.

ENM−Cellular Interactions: Reduction of Toxicity for the Case of CeO_2. No toxicity was observed in vitro for either bare CeO_2, or the SiO_2-coated CeO_2 with the A549 cell line (Figure 7a and b). Therefore, the reduction of toxicity in vitro could not be made for the case of SiO_2-coated CeO_2 given the fact that the uncoated CeO_2 ENMs exhibited minimal toxicity. The authors recognize that additional in vitro assays, testing various end points across different cell lines, may improve sensitivity for detecting toxicity in vitro beyond the LDH and MTT assays reported here for A549 cells. However, several studies investigating the in vitro toxicity of CeO_2 across a broad range of cell lines from various tissues and examining a variety of biological end points have already been reported in the literature and found CeO_2 to be relatively nontoxic across the board.[49,58,59] Kroll et al. reported CeO_2 ENMs do not induce cytotoxicity measured by LDH and MTT assays and do not increase oxidative stress or generation of reactive oxygen species as measured by the DCF assay. These results were consistent across multiple cell lines including A549 cells, heterogeneous human epithelial colorectal adenocarcinoma cells (Caco-2), adenocarcinoma derived human lung epithelial cells (Calu-3), canine kidney epithelial cells (MDCK, MDCK II), mouse derived fibroblast cells (NIH-3T3), rat kidney cells (NRK52E), rat alveolar macrophages (RAW 264.7), and rat lung epithelial-T-antigen negative cells (RLE-6TN).[58] Similarly, Zhang et al. reported no toxicity and minimal oxidative stress for multiple cell lines exposed to CeO_2 ENMs (human bronchial epithelial cells (BEAS-2B) and rat alveolar macro-phages (RAW 264.7)).[49] Xia et al. investigated inflammatory cytokine release in response to CeO_2 exposure in vitro and reported no increase in TNF-α production after the ENMs are internalized by rat alveolar macrophages (RAW 264.7) and no IL-8 production after they are internalized by noncancerous human bronchial epithelial cells (BEAS-2B).[59]

Despite the compelling in vitro evidence presented above for the minimal toxicological properties of uncoated CeO_2, in vitro assays only provide limited information for realistic exposure risk assessment and are not necessarily in agreement with in vivo animal studies. Whole-animal in vivo inhalation studies are the "gold standard" for pulmonary toxicology due to their physiologically relevant exposure mechanisms and discrep-ancies with reported toxicity results in vitro highlight major

Table 2. Relevant Synthesis Parameters for Particles Presented in Figure 1c–f[a]

TEM figures	precursor	solvent	precursor molarity	$\dot{n}_{HMDSO}/\dot{n}_{core}$
Figure 1c	zinc naphthenate, 65% mineral spirits (10% Zn) (STREM)	ethanol (95%, Sigma Aldrich)	0.5	0.2
Figure 1d	zinc naphthenate, 65% mineral spirits (10% Zn) (STREM)	xylene (>99%, Sigma Aldrich)	0.5	0.2
Figure 1e and f	zinc naphthenate, 65% mineral spirits (10% Zn) (STREM)	ethanol (95%, Sigma Aldrich)	0.5	0.41

[a]Parameters which are not listed were not changed and are as described in the Materials and Methods section.

concerns about the predictive capacity for cellular nanotoxicology studies.

In the case of CeO_2, several recent studies report large discrepancies between in vitro models and more realistic in vivo models for CeO_2 ENMs. Recent instillation studies measuring pulmonary toxicity in rats have reported significant pulmonary toxicity for CeO_2 ENMs.[61,62]

In another recently published study performed by our group, Sprague–Dawley rats were exposed via inhalation to either CeO_2 or SiO_2 encapsulated CeO_2 ENMs in order to assess the toxicological impact of SiO_2 encapsulation in vivo.[63] Animals exposed to bare CeO_2 exhibited eight times greater inflammation, as measured by influx of polymorphonuclear leukocytes in the bronchoalveolar lavage fluid (BALF), than those exposed to the SiO_2-coated ENMs. Additionally, reported LDH release was significantly elevated in the BALF of rats exposed to bare CeO_2 compared with those exposed to SiO_2-coated CeO_2. For both outcomes measured, the SiO_2-encapsulated CeO_2 ENMs induced minimal pulmonary toxicity and was comparable to the particle-free control, thereby supporting the proposed safer formulations concept (Supporting Information Figure S-4).

ENM–Cellular Interactions: Fe_2O_3 and Ag. Similar to the bare CeO_2, SiO_2, and SiO_2-coated ENMs, no toxicity was observed in vitro for either the bare Fe_2O_3 or the Ag with the A549 cell line (Figures 7a and b). Therefore, making any conclusion based solely on in vitro evidence for the SiO_2-coated materials is not possible. These findings for minimal in vitro toxicity in mammalian epithelial cells are consistent with results reported in the literature for pure Fe_2O_3, and Ag ENMs at the employed nanoparticle sizes and measured concentrations across various cell lines and measured biological end points.[49,58,59,64]

It is again important to note that in vitro assays only provide limited information for realistic exposure risk assessment, and several recent studies report large discrepancies between in vitro models and more realistic in vivo models.[13,17–19,65] For example, while Fe_2O_3 exhibited minimal toxicity on A549 cells evaluated in this study, a recent in vivo study by the authors, suggests that moderate and acute exposure to Fe_2O_3 nanoparticles can cause lung injury and inflammation in Sprague–Dawley rats.[28] With regards to Ag, limited data is available for in vivo pulmonary toxicity. One group reported inhalation exposure to 18 nm silver particles resulted in decreased lung function (including tidal volume, minute volume, and peak inspiration flow), as well as inflammatory lesions in the lung morphology and increased inflammatory markers during a 90 day rat study.[66] Considering the relatively mild effects reported for SiO_2 in vivo, we expect the SiO_2 coated Fe_2O_3 and Ag to demonstrate decreased toxicity in vivo as well, similar to the protective effects observed for ZnO and CeO_2. Again, conflicting evidence between in vitro and in vivo studies highlight limitations in current in vitro protocols at predicting toxicity and emphasize the need for biologically complex and physiologically relevant exposure systems in vitro.[61–63]

The authors recognize the need to further study in vivo the effect of SiO_2 coating on these ENMs, and plans are underway to generate in vivo data on the effect of SiO_2 coating on their toxicity. However, our compelling in vitro and in vivo evidence presented here for the case of SiO_2 coated CeO_2 and ZnO as well as data on the biologically inert nature of amorphous SiO_2 reported in the literature suggests hermetic encapsulation with amorphous SiO_2 is an appropriate safer formulation approach.

CONCLUSIONS

In summary, we showcase the effectiveness of a novel safer formulation concept for flame-generated ENMs by applying it to a comprehensive and industry-relevant nanopanel. The versatile and scalable process described here enables the one step, inflight, hermetic encapsulation of potentially toxic ENMs by a nanothin SiO_2 layer. An effective technique for quantitatively assessing the coating efficiency of the SiO_2-encapsulation process based on XPS was also presented and validated. Finally, we provide valuable in vitro and in vivo toxicological evidence for the ability of the proposed concept to reduce the toxicological profile of the ENMs, while maintaining the functional properties of the core materials. The optimum theoretical SiO_2 coating thickness for each nanoparticle type sufficient to render core materials hermetically coated and therefore nontoxic is greater than 2 nm. The TEM imaging confirms an approximate 3 nm coating thickness, but it is semiquantitative. The described concept bears great promise for large-scale industrial application as a means of effectively inhibiting nanoparticle toxicity.

MATERIALS AND METHODS

ENM Synthesis. The synthesis of the bare and SiO_2-coated nanoparticles was performed using the flame spray pyrolysis (FSP) based Harvard versatile engineered nanomaterial generation system (VENGES[27,28]). In brief, Fe_2O_3, Ag, ZnO, CeO_2, and core particles were synthesized by combustion of organometallic precursors listed in Table 2. Precursor solutions were fed to the FSP nozzle through a stainless steel capillary at 5 mL/min, dispersed by 5 L/min O_2 (Air Gas, purity >99%, pressure drop at nozzle tip: p_{drop} = 2 bar) and combusted to form the desired nanomaterials. A premixed stoichiometric methane–oxygen (1.5 and 3.2 L/min) supporting flame was used along with 40 L/min O_2 (Air Gas, purity >99%) sheath gas.

The FSP burner was enclosed with a 200 mm quartz glass tube (i.d. 45 mm). On top of this tube, HMDSO (Sigma Aldrich) vapor was swirl-injected through a torus ring with 16 equidistant and of equal size (d_{inner} = 0.6 mm) openings. A total gas flow of 16 L/min, consisting of N_2 carrying HMDSO vapor ($V_{N2,coat}$) and pure N_2 ($V_{N2,swirl}$) for mixing, was injected through the torus ring jets. The torus ring jet injection angles were 20° in the downstream direction, in order to avoid stagnation flow, and 10° away from the centerline, in order to induce the necessary mixing swirl.[67] The reactor was terminated by a 200–400 mm quartz tube. HMDSO vapor was obtained by bubbling N_2 ($V_{N2,coat}$) gas through liquid HMDSO (500 mL), maintained at a controlled temperature using a temperature-controlled water bath. At saturated conditions, the HMDSO content within the $N_{2,coat}$ flow is determined by the HMDSO partial vapor pressure, which is a function

of the bubbler temperature and can be estimated using the Antoine equation.[31] We define the molar ratio of injected HMDSO to synthesized core particles as $\dot{n}_{HMDSO}/\dot{n}_{core}$. A theoretical coating thickness (TCT) for the individual particles was estimated based on $\dot{n}_{HMDSO}/\dot{n}_{core}$, assuming full HMDSO conversion to SiO_2 coatings (no separate SiO_2 formation)[31] as well as monodisperse spherical primary particles of a known diameter (d_{XRD}).

The bare nanoparticles were synthesized at identical conditions, in the absence, however, of the HMDSO vapor. For the purpose of evaluating ENM−biological interactions, bare Ag was cooxidized with SiO_2, in order to provide sufficient control over Ag primary particle size.[18] After synthesis, particles were collected for physicochemical characterization and in vitro toxicity assessments on a water-cooled glass fiber filter (Whatman) located 800 mm above the reactor.[27,28] A schematic of the coating reactor used is provided in Figure 1.

■ PHYSICOCHEMICAL CHARACTERIZATION

Structure, Composition, Morphology. X-ray diffraction (XRD) patterns for ZnO and CeO_2 were obtained using a Scintag XDS2000 powder diffractometer (Cu Kα (λ = 0.154 nm), −40 kV, 40 mA, stepsize = 0.02°). The crystal size was determined by applying the Sherrer shape equation to the Gaussian fit of the major diffraction peak. Fe_2O_3 and Ag XRD patterns were obtained using a Bruker D8 diffractometer (Cu Kα (λ = 0.154 nm), −40 kV, 40 mA, stepsize = 0.02°). The crystal size was determined by Rietveld analysis, and the crystal size of the major diffraction peak is reported. The Brunauer−Emmett−Teller (BET) powder-specific surface area (SSA) of all samples was measured by N_2 adsorption at 77 K (Micromeritics TriStar), after sample degassing for 1 h at 150 °C in nitrogen. ENMs were also deposited onto carbon grids for TEM imaging (TEM: Libra 120).

Coating Efficiency Characterization. Highly surface sensitive X-ray photoelectron spectroscopy (XPS) (ESCA SSX-100; X-ray source monochromatic Al Kα, 10 kV, 10 mA; detector hemispherical electron energy spectrometer; spot size 600 μm) was used to assess SiO_2 coating efficiency. Survey scans (binding energy range 0−1100 eV, pass energy 100 eV, step size 0.65 eV) were used for surface elemental quantification. All XPS spectra were calibrated using the C1s hydrocarbon contamination peak (BE 284.6 eV). Atomic concentrations were determined using CASA XPS software and respective sensitivity factors for relevant elements.

XPS results were supported by isopropanol chemisorption on SiO_2 coated and bare CeO_2 particles following methods described previously.[19,32] In brief, 50 mg of sample were heated at 10 °C/min to 400 °C and kept there for 30 min in a 20% O_2 atmosphere (50 mL/min) to remove surface water and carbonaceous species. Samples were then cooled to 110 °C and flushed with He for 10 min. 2-Propanol (2000 ppm; Messer) in N_2 (50 mL/min) was then introduced at 110 °C for 30 min to minimize physisorption and optimize chemisorption of the 2-propoanol. The gas atmosphere was again changed to He, and after 10 min the sample was heated at 10 °C/min to 500 °C. During this final heating stage, the thermal conductivity of off-gases was monitored by an Autochem II 2920 thermal conductivity detector (Micromeritics, Georgia).

Additional photocatalytic experiments were conducted for ZnO and SiO_2-coated ZnO nanoparticles. In brief, 18 mg of the ZnO or SiO_2-coated ZnO nanoparticles were added in 100 mL of a 10 ppm methylene blue aqueous solution. The suspension was sonicated for 20 s with a Branson Sonifier S-450A (Branson Ultrasonics, Danbury, CT) fitted with a 3 in. cup horn (maximum power output of 400 W at 60 Hz, continuous mode,

output level 3), and left in the dark for 20 min. The suspension then was irradiated with an 8 W 254 nm UV lamb for 1 h, and 1 mL samples were collected after 10, 20, 45, and 60 min. The samples were placed in 2 mL centrifuge tubes and were spun at 20 000 rpm. The supernatant was removed and the adsorption spectrum was measured with the Synergy 2 Multi-Mode microplate reader (Biotek Instruments, Winooski, VT) from 550 to 700 nm. The intensity of three wavelengths (615, 630, and 660 nm) was measured with reference at 700 nm. The data were plotted normalized to the initial concentration (C_i/C_0) where C_0 is the concentration at t = 0 and C_i is the concentration at a given time. The data were fit with an exponential decay $C_i/C_0 = \exp(-t/\tau_0)$.

ENM Dispersal and Characterization in Liquid. ENM dispersion was performed using a protocol previously described[44] and included the calibration of sonication equipment and standardized reporting of sonication energy. We identified for each ENM the material-specific critical sonication energy required to achieve monodisperse solutions at the lowest agglomeration state as measured by dynamic light scattering (DLS). Cup horn sonication was performed in deionized water (DI H_2O) to minimize reactive oxygen species generation via sonolysis, to minimize ionic strength and specific conductance, and hence particle interactions, during sonication, and to avoid denaturation of proteins in the final cell delivery media. Stock solutions in DI H_2O were then diluted to desired concentrations (0, 6.25, 12.5, 25, or 50 μg/mL) in F-12K cell culture media supplemented with 3% heat-inactivated fetal bovine serum (FBS), 100 U/ml penicillin, 100 μg/mL streptomycin, and 10 mM HEPES (F-12K/3%FBS) and vortexed for 30 s. ENM suspensions in F-12K/3% FBS were then characterized for hydrodynamic diameter (d_H), polydispersity index (PdI), zeta potential (ζ), and specific conductance (σ) by dynamic light scattering (DLS) using a Zetasizer Nano-ZS (Malvern Instruments, Worcestershire, UK). pH was also measured using a VWR sympHony pH meter (VWR International, Radnor, PA, USA). Following comprehensive characterization, dispersions were applied to cells for toxicological evaluation.

The critical delivered sonication energy (DSE_{cr}) was determined for each ENM as follows. ENMs were dispersed at 1 mg/mL in 10 mL of solute in 50 mL, 24 mm diameter conical polyethylene tubes, by sonication with a Branson Sonifier S-450A (Branson Ultrasonics, Danbury, CT) fitted with a 3 in. cup horn (maximum power output of 400 W at 60 Hz, continuous mode, output level 3). The tube was immersed so that the sample liquid aligned with the level of water in the cup. The system was calibrated by the calorimetric calibration method previously described,[44,68] whereby the power delivered to the sample was determined to be 1.75 W. Dispersions were analyzed by DLS, and hydrodynamic diameter as a function of DSE exhibiting asymptotic deagglomeration trends were derived for each ENM. From each curve, an ENM-specific DSE_{cr} was estimated by determining the DSE value at which the dispersed ENMs were within 10% of their observed minimum d_H value (theoretical d_H at DSE = +∞).

Absorbance of ZnO and SiO_2-coated ZnO particles dispersed in DI H_2O was measured at 5 nm intervals across a spectrum of wavelengths ranging from 315 to 800 nm using a Spectramax Multi-Mode microplate reader (Molecular Devices, USA).

In-Vitro Toxicity. *Cell Lines.* Human alveolar basal epithelial A549 cells were cultured in F-12/K supplemented with 10% heat-inactivated fetal bovine serum (FBS), 100 U/mL

854

dx.doi.org/10.1021/sc300152f | ACS Sustainable Chem. Eng. 2013, 1, 843−857

penicillin, 100 μg/mL streptomycin, and 10 mM HEPES. All incubations were performed at 37 °C/5% CO_2 unless otherwise specified. Assays were repeated three times for each ENM. F-12/K cell culture media, penicillin/streptomycin, HEPES, and BSA were obtained from Sigma Aldrich (St. Louis, MO), and FBS and heat-inactivated FBS were obtained from Atlanta Biologicals (Atlanta, GA).

Bioassays. Cellular metabolic activity and cytotoxicity were measured via the 3-(4,5-dimethylthiazol-2-yl)-2,5-diphenylte-trazolium bromide (MTT) assay and lactate dehydrogenase (LDH) assay respectively according to the standard protocols. In short, cells were seeded in 96-well microtiter plates (Corning Inc., New York, NY) at a concentration of 1×10^5 cells per well. The next day, culture media was replaced with 100 μL of ENM dispersions in either F-12K/3%FBS at various concentrations and incubated for 24 h. Following 24 h of exposure, 50 μL of supernatant was collected and transferred to fresh 96-well plates and 100 μL of LDH-reagent was applied. These plates were then left for 30 min in the dark at room temperature. During this incubation period, the presence of LDH released by dead or dying cells into the supernatant due to plasma membrane damage was identified by the reduction of the reagent tetrazolium salt, measurable by absorbance. Plates were read immediately following incubation at 490 nm with a Synergy 2 Multi-Mode microplate reader (Biotek Instruments, Winooski, VT).

Exposure media was removed from the plates still containing cells, replaced with fresh medium containing MTT reagent, and incubated for an additional 4 h. Vital cells integrated the dye and transformed the yellow tetratzolium salt (MTT) into purple formazan crystals, an indicator of active metabolism. Following the 4-h incubation period, 100 μL of MTT solubilization solution (10% Triton X-100 with 0.1 N HCl in anhydrous isopropanol) were added to the wells to stop the reaction. Plates were placed on an orbital plate shaker for 30 min to dissolve the formazan crystals and, then, centrifuged at 250 rpm for 10 min to ensure that particles or dying cells were removed from the solution. A 100 μL portion of the supernatant was then removed and placed in a fresh 96 well plate to be read at 570 nm with a Synergy 2 Multi-Mode microplate reader (Biotek Instruments, Winooski, VT). MTT cell proliferation kits and LDH cytotoxicity detection kits were obtained from Roche Applied Science (Indianapolis, IN). All experiments were conducted in triplicate for each ENM.

Calculations and Statistics. Abosrbance values measured for LDH and MTT in vitro assays were normalized with negative control (particle free media) and positive control (Triton X) absorbance values, to a metric of cell viability (%) using the following equation:

cell viability (%) =

(sample absorbance − negative control absorbance)/

(positive control absorbance − negative control absorbance)

Statistics. Variance of toxicity results for each ENM was tested by post hoc one-way ANOVA with significance set at $p \leq 0.05$. One-tailed unpaired student t test was used for significance testing, with significance set at $p \leq 0.05$.

■ ASSOCIATED CONTENT

Ⓢ Supporting Information

Supplemental Figures 1−4: optical absorbance of the ZnO nanoparticles, the VENGES used for the in vivo inhalation studies, the XRD patterns of the ZnO nanoparticles, and the in vivo toxicity data for CeO_2 and SiO_2-coated CeO_2 ENMs. Supplemental Table 1: all precursor information. This material is available free of charge via the Internet at http://pubs.acs.org.

■ AUTHOR INFORMATION

Corresponding Author

*E-mail: pdemokri@hsph.harvard.edu.

Notes

The authors declare no competing financial interest.

■ REFERENCES

(1) Spibey, C., Ed. *2010 Nanotechnology Research Review*; BCC Research Market Forecasting: Wellesley, MA, 2011.

(2) MacWilliams, A., Ed. *Nanotechnology: A Realistic Market Assessment*; BCC Research Market Forecasting: Wellesley, MA, 2010.

(3) Dowling, A., Ed. *Nanoscience and Nanotechnologies: Opportunities and Uncertainties*; The Royal Society and the Royal Academy of Engineering: London, 2004.

(4) *The Nanotechnology Consumer Product Inventory*. http://www.nanotechproject.org/inventories/consumer/ (accessed Jan 2013).

(5) Lewinski, N.; Colvin, V.; Drezek, R. Cytotoxicity of nanoparticles. *Small* **2008**, *4*, 26−49.

(6) Bello, D.; Martin, J.; Santeufemio, C.; Sun, Q.; Lee Bunker, K.; Shafer, M.; Demokritou, P. Physicochemical and morphological characterisation of nanoparticles from photocopiers: implications for environmental health. *Nanotoxicology* **2012**, DOI: 10.3109/17435390.2012.689883.

(7) Nel, A.; Xia, T.; Madler, L.; Li, N. Toxic potential of materials at the nanolevel. *Science* **2006**, *311*, 622−7.

(8) Hamilton, R. F.; Wu, N.; Porter, D.; Buford, M.; Wolfarth, M.; Holian, A. Particle length-dependent titanium dioxide nanomaterials toxicity and bioactivity. *Part. Fibre Toxicol.* **2009**, *6*, 35.

(9) Larsen, S. T.; Roursgaard, M.; Jensen, K. A.; Nielsen, G. D. Nano titanium dioxide particles promote allergic sensitization and lung inflammation in mice. *Basic Clin. Pharmacol. Toxicol.* **2010**, *106*, 114−7.

(10) Li, J. J.; Muralikrishnan, S.; Ng, C. T.; Yung, L. Y.; Bay, B. H. Nanoparticle-induced pulmonary toxicity. *Exp. Biol. Med. (Maywood)* **2010**, *235*, 1025−33.

(11) Poland, C. A.; Duffin, R.; Kinloch, I.; Maynard, A.; Wallace, W. A.; Seaton, A.; Stone, V.; Brown, S.; Macnee, W.; Donaldson, K. Carbon nanotubes introduced into the abdominal cavity of mice show asbestos-like pathogenicity in a pilot study. *Nat. Nanotechnol.* **2008**, *3*, 423−8.

(12) Xia, T. A.; Zhao, Y.; Sager, T.; George, S.; Pokhrel, S.; Li, N.; Schoenfeld, D.; Meng, H. A.; Lin, S. J.; Wang, X.; Wang, M. Y.; Ji, Z. X.; Zink, J. I.; Madler, L.; Castranova, V.; Lin, S.; Nel, A. E. Decreased Dissolution of ZnO by Iron Doping Yields Nanoparticles with Reduced Toxicity in the Rodent Lung and Zebrafish Embryos. *ACS Nano* **2011**, *5*, 1223−1235.

(13) George, S.; Pokhrel, S.; Xia, T.; Gilbert, B.; Ji, Z. X.; Schowalter, M.; Rosenauer, A.; Damoiseaux, R.; Bradley, K. A.; Madler, L.; Nel, A. E. Use of a Rapid Cytotoxicity Screening Approach To Engineer a Safer Zinc Oxide Nanoparticle through Iron Doping. *ACS Nano* **2010**, *4*, 15−29.

(14) Jin, Y. H.; Kannan, S.; Wu, M.; Zhao, J. X. J. Toxicity of luminescent silica nanoparticles to living cells. *Chem. Res. Toxicol.* **2007**, *20*, 1126−1133.

(15) Teleki, A.; Heine, M. C.; Krumeich, F.; Akhtar, M. K.; Pratsinis, S. E. In situ coating of flame-made TiO_2 particles with nanothin SiO_2 films. *Langmuir* **2008**, *24*, 12553−8.

(16) Teleki, A.; Suter, M.; Kidambi, P. R.; Ergeneman, O.; Krumeic, F.; Nelson, B. J.; Pratsinis, S. E. Hermetically coated superparamagnetic Fe_2O_3 particles with SiO_2 nanofilms. *Chem. Mater.* **2009**, *21*, 6.

(17) Sotiriou, G. A.; Hirt, A. M.; Lozach, P. Y.; Teleki, A.; Krumeich, F.; Pratsinis, S. E. Hybrid, Silica-Coated, Janus-like Plasmonic-Magnetic Nanoparticles. *Chem. Mater.* **2011**, *23*, 7.

(18) Sotiriou, G. A.; Sannomiya, T.; Teleki, A.; Krumeich, F.; Voros, J.; Pratsinis, S. E. Non-toxic dry-coated nanosilver for plasmonic biosensors. *Adv. Funct. Mater.* **2010**, *20*, 7.

(19) Sotiriou, G. A.; Franco, D.; Poulikakos, D.; Ferrari, A. Optically Stable Biocompatible Flame-Made SiO_2-Coated Y_2O_3: Tb^{3+} Nanophosphors for Cell Imaging. *ACS Nano* **2012**, *6*, 9.

(20) Wegner, K.; Pratsinis, S. E. Scale-up of Nanoparticle Synthesis in Diffusion Flame Reactors. *Chem. Eng. Sci.* **2003**, *58*, 9.

(21) Pratsinis, S. E. Flame aerosol synthesis of ceramic powders. *Prog. Energy Combust. Sci.* **1998**, *24*, 23.

(22) Pratsinis, S. E. Aerosol-based Technologies in Nanoscale Manufacturing: from Functional Materials to Devices through Core Chemical Engineering. *AIChE J.* **2010**, *56*, 3028−3035.

(23) Stober, W.; Fink, A.; Bohn, E. Controlled growth of monodisperse silica spheres in the micron size range. *J. Colloid Interface Sci.* **1968**, *26*, 7.

(24) Kobayashi, Y.; Katakami, H.; Mine, E.; Nagao, D.; Konno, M.; Liz-Marzan, L. M. Silica coating of silver nanoparticles using a modified Stober method. *J. Colloid Interface Sci.* **2005**, *283*, 4.

(25) Han, Y.; Jian, J.; Lee, S. S.; Ying, J. Y. Reverse microemulsion-mediated synthesis of silica-coated gold and silver nanoparticles. *Langmuir* **2008**, *24*, 6.

(26) Xu, K.; Wang, J. X.; Kang, X. L.; Chen, J. F. Fabrication of antibacterial monodispersed Ag-SiO_2 core-shell nanoparticles with high concentration. *Mater. Lett.* **2009**, *63*, 3.

(27) Demokritou, P.; Buchel, R.; Molina, R. M.; Deloid, G. M.; Brain, J. D.; Pratsinis, S. E. Development and characterization of a Versatile Engineered Nanomaterial Generation System (VENGES) suitable for toxicological studies. *Inhal. Toxicol.* **2010**, *22* (Suppl 2), 107−116.

(28) Sotiriou, G. A.; Diaz, E.; Long, M. S.; Godleski, J.; Brain, J.; Pratsinis, S. E.; Demokritou, P. A novel platform for pulmonary and cardiovascular toxicological characterization of inhaled engineered nanomaterials. *Nanotoxicology* **2011**, *11*, 680−690.

(29) Schrand, A. M.; Rahman, M. F.; Hussain, S. M.; Schlager, J. J.; Smith, D. A.; Syed, A. F. Metal-based nanoparticles and their toxicity assessment. *WIREs Nanomed. Nanobiotechnol.* **2010**, *2*, 544−568.

(30) Strobel, R.; Pratsinis, S. E. Flame Aerosol Synthesis Of Smart Nanostructured Materials. *J. Mater. Chem.* **2007**, *17*, 14.

(31) Teleki, A.; Buesser, B.; Heine, M. C.; Krumeich, F.; Akhtar, M. K.; Pratsinis, S. E. Role of Gas-Aerosol Mixing during in Situ Coating of Flame-Made Titania Particles. *Ind. Eng. Chem. Res.* **2009**, *48*, 85−92.

(32) Teleki, A.; Akhtar, M. K.; Pratsinis, S. E. The quality of SiO2-coatings on flame-made TiO2-based nanoparticles. *J. Mater. Chem.* **2008**, *18*, 9.

(33) Sotiriou, G. A.; Schneider, M.; Pratsinis, S. E. Green, Silica-Coated Monoclinic Y_2O_3:Tb^{3+} Nanophosphors: Flame Synthesis and Characterization. *J. Phys. Chem. C* **2012**, *116*, 6.

(34) Buesser, B.; Pratsinis, S. E. Design of aerosol particle coating: Thickness, texture and efficiency. *Chem. Eng. Sci.* **2010**, *65*, 5471−5481.

(35) Warheit, D. B.; McHugh, T. A.; Hartsky, M. A. Differential pulmonary responses in rats inhaling crystalline, colloidal or amorphous silica dusts. *Scand. J. Work Environ. Health* **1995**, *21* (Suppl 2), 19−21.

(36) Brundle, C.; Evans, C. A.; Wilson, S. *Encyclopedia of Materials Characterization: Surfaces, Interfaces, Thin Films*; Butterworth-Heinemann: Boston, 1992

(37) Hellwig, M.; Parala, H.; Cybinksa, J.; Barreca, D.; Gasparotto, A.; Niermann, B.; Becker, H. W.; Rogalla, D.; Feydt, J.; Irsen, S.; Mudring, A. V.; Winter, J.; Fischer, R. A.; Devi, A. Atomic vapor deposition approach to In_2O_3 thin films. *J. Nanosci. Nanotechnol.* **2011**, *11*, 8094−100.

(38) Vemuri, R. S.; Engelhard, M. H.; Ramana, C. V. Correlation between surface chemistry, density, and band gap in nanocrystalline WO_3 thin fimls. *ACS Appl. Mater. Interfaces* **2012**, *4*, 7.

(39) Jung, R.; Lee, J. C.; Orosz, G. T.; Sulyok, A.; Zsolt, G.; Menyhard, M. Determination of effective electron inelastic mean free paths in SiO_2 and Si_3N_4 using a Si reference. *Surf. Sci.* **2003**, *543*, 9.

(40) Garcia, R.; Kubicek, V.; Drahos, B.; Gano, L.; Santos, I. C.; Campello, P.; Paulo, A.; Toth, E.; Santos, I. Synthesis, characterization and biological evaluation of In(III) complexes anchored by DOTA-like chelators bearing a quinazoline moiety. *Metallomics* **2010**, *2*, 571−80.

(41) Kulkarni, D.; Wachs, S. E. Isopropanol oxidation by pure metal oxide catalysts: number of active surface sites and turnover frequencies. *Appl. Catal., A* **2002**, *237*, 16.

(42) Zhou, Y. C.; Rahaman, M. N. Hydrothermal synthesis and sintering of ultrafine CeO_2 powders. *J. Mater. Res.* **1993**, *8*, 7.

(43) Height, M. J.; Pratsinis, S. E.; Mekasuwandumrong, O.; Praserthdam, P. Ag-ZnO catalysts for UV-photodegradation of methylene blue. *Appl. Catal. B: Environ.* **2006**, *63*, 8.

(44) Cohen, J.; DeLoid, G.; Pyrgiotakis, G.; Demokritou, P. Interactions of Engineered Nanomaterials in Physiological Media and Implications for In Vitro Dosimetry. *Nanotoxicology* **2012**, DOI: 10.3109/17435390.2012.666576.

(45) Raming, T. P.; Winnubst, A. J. A.; van Kats, C. M.; Philipse, A. P. The Synthesis and Magnetic Properties of Nanosized Hematite (α-Fe_2O_3) Particles. *J. Colloid Interface Sci.* **2002**, *249*, 5.

(46) Laurent, S.; Mahmoudi, M. Superparamagnetic iron oxide nanoparticles: promises for diagnosis and treatment of cancer. *Int. J. Mol. Epidemiol. Genet.* **2011**, *2*, 24.

(47) Amin, N.; Arajs, S. Morin temperature of annealed submicronic α-F_2O_3 particles. *Phys. Rev. B* **1987**, *35*, 2.

(48) George, S.; Xia, R.; Rallo, R.; Zhao, Y.; Ji, Z.; Lin, S.; Wang, X.; Zhang, H.; France, B.; Schoenfeld, D.; Damoiseaux, R.; Liu, R.; Lin, S.; Bradley, K. A.; Cohen, Y.; Nel, A. E. Use of a High-Throughput Screening Approach Coupled with In Vivo Zebrafish Embryo Screening to Develop Hazard Ranking for Engineered Nanomaterials. *ACS Nano* **2011**, *5*, 13.

(49) Zhang, H.; Ji, Z.; Xia, T.; Meng, H.; Low-Kam, C.; Liu, R.; Pokhrel, S.; Lin, S.; Wang, X.; Liao, Y. P.; Wang, M.; Li, L.; Rallo, R.; Damoiseaux, R.; Telesca, D.; Madler, L.; Cohen, Y.; Zink, J. I.; Nel, A. E. Use of metal oxide nanoparticle band gap to develop a predictive paradigm for oxidative stress and acute pulmonary inflammation. *ACS Nano* **2012**, *6*, 4349−68.

(50) Murashov, V.; Harper, M.; Demchuk, E. Impact of silanol surface density on the toxicity of silica aerosols measured by erythrocyte haemolysis. *J. Occup. Environ. Hyg.* **2006**, *3*, 718−23.

(51) Fubini, B.; Zanetti, G.; Altilia, S.; Tiozzo, R.; Lison, D.; Saffiotti, U. Relationship between surface properties and cellular responses to crystalline silica: studies with heat-treated cristobalite. *Chem. Res. Toxicol.* **1999**, *12*, 9.

(52) Napierska, D.; Thomassen, L. C.; Lison, D.; Martens, J. A.; Hoet, P. H. The nanosilica hazard: another variable entity. *Part. Fibre Toxicol.* **2010**, *7*, 39.

(53) Sayes, C. M.; Reed, K. L.; Glover, K. P.; Swain, K. A.; Ostraat, M. L.; Donner, E. M.; Warheit, D. B. Changing the dose metric for inhalation toxicity studies: short-term study in rats with engineered aerosolized amorphous silica nanoparticles. *Inhal. Toxicol.* **2010**, *22*, 348−54.

(54) Lee, K. P.; Kelly, D. P. The pulmonary response and clearance of Ludox colloidal silica after a 4-week inhalation exposure in rats. *Fundam. Appl. Toxicol.* **1992**, *19*, 399−410.

(55) Reuzel, P. G.; Bruijntjes, J. P.; Feron, V. J.; Woutersen, R. A. Subchronic inhalation toxicity of amorphous silicas and quartz dust in rats. *Food Chem. Toxicol.* **1991**, *29*, 341−54.

(56) Rosenbruch, M. Inhalation of amorphous silica: morphological and morphometric evaluation of lung associated lymph nodes in rats. *Exp. Toxicol. Pathol.* **1992**, *44*, 10−4.

(57) Mueller, R.; Kammler, H. K.; Wegner, K.; Pratsinis, S. E. OH Surface Density of SiO_2 and TiO_2 by Thermogravimetric Analysis. *Langmuir* **2003**, *19*, 6.

(58) Kroll, A.; Dierker, C.; Rommel, C.; Hahn, D.; Wohlleben, W.; Schulze-Isfort, C.; Gobbert, C.; Voetz, M.; Hardinghaus, F.; Schnekenburger, J. Cytotoxicity screening of 23 engineered nanomaterials using a test matrix of ten cell lines and three different assays. *Part. Fibre Toxicol.* **2011**, 8.

(59) Xia, T.; Kovochich, M.; Liong, M.; Madler, L.; Gilbert, B.; Shi, H.; Yeh, J. I.; Zink, J. I.; Nel, A. E. Comparison of the mechanism of toxicity of zinc oxide and cerium oxide nanoparticles based on dissolution and oxidative stress properties. *ACS Nano* **2008**, *2*, 2121−34.

(60) Sayes, C. M.; Reed, K. L.; Warheit, D. B. Assessing toxicity of fine and nanoparticles: comparing in vitro measurements to in vivo pulmonary toxicity profiles. *Toxicol. Sci.* **2007**, *97*, 163−80.

(61) Ma, J. Y.; Zhao, H. W.; Mercer, R. R.; Barger, M.; Rao, M.; Meighan, T.; Schwegler-Berry, D.; Castranova, V.; Ma, J. K. Cerium oxide nanoparticle-induced pulmonary inflammation and alveolar macrophage functional change in rats. *Nanotoxicology* **2011**, *5*, 312−325.

(62) Nalabotu, S. K.; Kolli, M. B.; Triest, W. E.; Ma, J. Y.; Manne, N. D. P. K.; Katta, A.; Addagarla, H. S.; Rice, K. M.; Blough, E. R. Intratracheal instillation of cerium oxide nanoparticles induces hepatic toxicity in male Sprague-Dawley rats. *Int. J. Nanomed.* **2011**, *6*, 2327−2335.

(63) Demokritou, P.; Gass, S.; Pyrgiotakis, G.; Cohen, J. M.; Goldsmith, W.; McKinney, W.; Frazer, D.; Ma, J.; Schwegler-Berry, D.; Brain, J.; Castranova, V. An in vivo and in vitro toxicological characterization of realistic nanoscale CeO_2 inhalation exposures. *Nanotoxicology* **2012**, DOI: 10.3109/17435390.2012.739665.

(64) Park, S.; Lee, Y. K.; Jung, M.; Kim, K. H.; Chung, N.; Ahn, E. K.; Lim, Y.; Lee, K. H. Cellular toxicity of various inhalable metal nanoparticles on human alveolar epithelial cells. *Inhal. Toxicol.* **2007**, *19* (Suppl 1), 59−65.

(65) Zhang, T.; Stilwell, J. L.; Gerion, D.; Ding, L.; Elboudwarej, O.; Cooke, P. A.; Gray, J. W.; Alivisatos, A. P.; Chen, F. F. Cellular effect of high doses of silica-coated quantum dot profiled with high throughput gene expression analysis and high content cellomics measurements. *Nano Lett.* **2006**, *6*, 800−808.

(66) Sung, J. H.; Ji, J. H.; Yoon, J. U.; Kim, D. S.; Song, M. Y.; Jeong, J.; Han, B. S.; Han, J. H.; Chung, Y. H.; Kim, J.; Kim, T. S.; Chang, H. K.; Lee, E. J.; Lee, J. H.; Yu, I. J. Lung function changes in Sprague-Dawley rats after prolonged inhalation exposure to silver nanoparticles. *Inhal. Toxicol.* **2008**, *20*, 567−574.

(67) Hansen, J.; Jenson, J. R.; Livbjerg, H.; Johannessen, T. Synthesis of ZnO particles in a quench-cooled flame reactor. *AIChE J.* **2001**, *47*, 5.

(68) Taurozzi, J. S.; Hackley, V. A.; Wiesner, M. R. Ultrasonic dispersion of nanoparticles for environmental, health and safety assessment—issues and recommendations. *Nanotoxicology* **2011**, *5*, 711−729.

857

dx.doi.org/10.1021/sc300152f | ACS Sustainable Chem. Eng. 2013, 1, 843−857